Clim Dyn
DOI 10.1007/s00382-016-3167-7

A multi-model analysis of the resolution influence on precipitation climatology in the Gulf Stream region

Xuelei Feng[1,2] · Bohua Huang[1,2] · Ben P. Kirtman[3] · James L. Kinter III[1,2] · Long S. Chiu[1]

Received: 25 January 2016 / Accepted: 9 May 2016

Abstract Using climate simulations from coupled and uncoupled general circulation models, this study investigates the influence of horizontal resolution in both atmospheric and oceanic model components on the mean precipitation over the Gulf Stream (GS) region. For this purpose, three sets of model experiments are analyzed. The first two examine the effects of increasing horizontal resolution of an atmospheric general circulation model (AGCM) gradually from 100 to 10 km under fixed oceanic settings. Specifically, the AGCM is either forced with prescribed observed sea surface temperature (SST) (the first case) or coupled to a non-eddy-resolving ocean general circulation model (OGCM) at a fixed horizontal resolution near 100 km (the second case). The third set of experiments examines the effects of the oceanic resolution with a pair of long-term simulations by another coupled ocean–atmosphere general circulation model (CGCM), in which the OGCM is run respectively at non-eddy-resolving (100 km) and eddy-resolving (10 km) resolutions, while the AGCM resolution remains fixed at 50 km for both runs. In general, all simulations qualitatively reproduce the gross features of the mean GS precipitation and its annual cycle. At similar AGCM resolutions, the uncoupled models produce a GS rain band that is more realistic in both structure and strength compared to the coupled models with non-eddy-resolving oceans. This is because the prescribed observed SST better represents the gradient near the oceanic front than the non-eddy-resolving OGCMs simulate. An increase from the baseline AGCM resolution produces enhanced climatological GS precipitation, both large-scale and convective, with the latter more tightly confined to the oceanic front. The enhancement, however, is moderate and further increases in resolution achieves diminishing results. On the other hand, an increase in oceanic resolution from non-eddy-resolving to eddy resolving scheme results in more consistent simulations with observations in both intensity and structure of the rain band. The major increase is in the convective precipitation near the much-tightened SST gradient associated with the oceanic front. Therefore, the intensity improvement caused by oceanic resolution increases is more effective than that from atmospheric resolution increases. Further analyses show that the improvement of Gulf Stream precipitation climatology due to model horizontal resolution increases can be understood in terms of the atmospheric surface pressure adjustment to the sharper SST gradient near the oceanic front, which leads to stronger atmospheric surface convergence and upper level divergence. The associated ascending motion contributes to the precipitation band located in the Gulf Stream.

Keywords Precipitation climatology · Gulf Stream · Oceanic front · Atmospheric general circulation model · Eddy-resolving ocean general circulation model · Coupled ocean–atmosphere general circulation model · Model horizontal resolution

1 Introduction

The atmosphere and ocean are linked to each other by their exchanges of heat, fresh water, gases and momentum on a variety of temporal and spatial scales. Especially, the

✉ Bohua Huang
bhuang@gmu.edu

[1] Department of Atmospheric, Oceanic, and Earth Sciences, Mail Stop 6C5, George Mason University, 4400 University Drive, Fairfax, VA 22030, USA

[2] Center for Ocean-Land-Atmosphere Studies, George Mason University, Fairfax, VA, USA

[3] Rosenstiel School for Marine and Atmospheric Science, University of Miami, Coral Gables, FL, USA

Published online: 20 May 2016

air-sea interaction between the regional wind and sea surface temperature (SST) plays a critical role (Chelton and Xie 2010). Before the turn of this century, most analyses of the space–time variability of winds over the ocean were based on reports from sparse ship measurements. These ship observations in conjunction with coupled climate models having comparably coarse spatial resolution indicate a negative correlation between SST and local wind speed (Xie 2004) except in the tropics. This large-scale phenomenon can be explained as the oceanic response to wind-induced latent and sensible heat fluxes (Frankignoul 1985; Barsugli and Battisti 1998).

With the advance of satellite-based high-resolution remote sensing techniques, mid-latitude ocean–atmosphere coupling at oceanic mesoscales can be measured directly. As a result, a fundamentally different picture emerges of the air-sea interaction on the spatial scales of order 10–10^2 km than those larger than order 10^2 km. Using the wind fields measured by the QuickSCAT scatterometer and SST from the Advanced Microwave Scanning Radiometer (AMSR-E; Chelton and Wentz 2005) on the Earth Observing System Aqua satellite, O'Neill et al. (2005) first found a very strong positive correlation between wind and SST on the scales of 10–100 km over the Agulhas Return Current in the Southwest Indian Ocean. Thereafter, such potential SST forcing on local surface winds at mesoscales has been found in every region of strong SST fronts and active oceanic eddies from satellite observations (Chelton and Xie 2010).

One explanation of the positive SST-wind correlation on oceanic mesoscales, mostly associated with the oceanic eddies and fronts, is that an intensive increase in local SST reduces the static stability of the near-surface atmosphere, causing enhanced turbulent mixing that draws momentum from aloft to accelerate the surface wind (Xie 2004). Minobe et al. (2008) also point out that, in the marine boundary layer, the atmospheric pressure adjustments to sharp SST gradients leads to surface wind convergence. In general, this convergence is induced by winds across an SST front. On the other hand, winds parallel to the SST front generate additional vorticity. Both processes can be quantified by coupling coefficients between wind stress divergence (curl) and the downwind (crosswind) component of the SST gradient (Chelton and Xie 2010). More recently, Schneider and Qiu (2015) used a linear boundary layer model to examine the relative effects of the SST-induced atmospheric pressure and vertical mixing on a background Ekman flow. Their results show that surface divergence can be caused by either large-scale wind or thermal circulation across the front. On the other hand, the wind stress curl generated by the SST front is weakened by geostrophic spin down.

Recent studies (e.g., Bryan et al. 2010) have demonstrated that the frontal scale ocean–atmosphere interaction can be realistically simulated by coupled ocean–atmosphere general circulation models (CGCM) if the model resolution is high enough, especially, if the oceanic component is eddy resolving. A more critical question is whether such vigorous air-sea interaction on oceanic mesoscale eddies and fronts has significant influence on the larger scale atmospheric and oceanic general circulation. Recent developments in supercomputing technology have made it possible to conduct climate simulations at high resolution to examine the importance of the scale interactions (e.g., Kinter et al. 2013). However, how to utilize the increasing computational resources most efficiently to improve climate simulations is still a major challenge. A number of studies have investigated the influence of horizontal resolution on simulated climate by resolving previously inaccessible finer-scale processes. Several recent studies have focused on the importance of atmospheric model resolution in climate simulation (e.g., May and Roeckner 2001; Brankovic and Gregory 2001; Pope and Stratton 2002; Kobayashi and Sugi 2004; Hack et al. 2006; Navarra et al. 2008; Gent et al. 2010). The reported results are still quite diverse, ranging from minor or no improvement to significant differences in the model mean state and variability, depending on the areas and phenomena examined. For oceanic high-resolution simulation, the current literature provides compelling evidence suggesting that an eddy-resolving ocean component model in a climate system will significantly impact the simulation of the large-scale climate (Kirtman et al. 2012).

In this paper, we assess the impacts of the horizontal resolutions in the atmosphere and ocean on the precipitation climatology in the Gulf Stream (GS) region in current climate models. The GS region has the most active mesoscale air-sea interactions that significantly affect the regional climate. In particular, the sharp SST fronts in the regions associated with the off-shore western boundary current induces low sea level pressure (SLP) over its warm flank and produces a tight band of precipitation (Sweet et al. 1981; Wai and Stage 1989; Warner et al. 1990; Song et al. 2006; Minobe et al. 2008, 2010). The enhanced surface baroclinicity also influences the Atlantic storm track (Nakamura et al. 2004). These effects of the intense oceanic front on the storm track pattern and intensity have been investigated using idealized aquaplanet experiments (e.g., Brayshaw et al. 2008; Sampe et al. 2010). More recently, Small et al. (2014) and Hand et al. (2014) have forced an uncoupled AGCM with horizontal resolutions at 50 and 100 km with spatially or temporally filtered SST data in the GS region. In this study, we concentrate on whether the current atmospheric and oceanic resolutions of climate models adequately represent the effects of the SST front on the mean precipitation in the GS region and how effectively an increase in the atmospheric and/or oceanic resolution can

improve the simulation. Ideally, these questions should be tackled using a single climate system through a series of sensitivity experiments with different oceanic and atmospheric resolutions under both coupled and uncoupled frameworks. However, given the tremendous resources required for such a project, no such extensive sensitivity experiment from a single system exists, as far as we know. In this paper, we demonstrate that useful information can be gained by analyzing the extensive resolution-related simulations from several coupled and uncoupled climate systems.

The rest of the paper is structured as follows. Section 2 introduces data and model configuration. Detailed results of resolution impacts on precipitation climatology in the Gulf Stream region are described in Sect. 3. Its physical mechanism is discussed in Sect. 4, and the summary, as well as concluding remarks, is provided in Sect. 5.

2 Simulations and observed data

We use existing climate model simulations from several major modeling projects to examine their simulated GS precipitation. Three sets of experiments are analyzed. The first two examine the effects of increasing AGCM horizontal resolution forced with observed SST or coupled to an OGCM at a given resolution. The third set examines the effects of the oceanic resolution with a pair of long-term simulations by another CGCM, with its OGCM configured at non-eddy-resolving and eddy-resolving resolutions respectively while its AGCM resolution remains fixed. These simulations are described below. The observational datasets used in this study are also described.

2.1 Athena atmospheric simulations

The sensitivity to the horizontal resolution of an AGCM forced with observed SST is studied using simulations from Project Athena (Kinter et al. 2013). This collaborative project brought together an international team of climate-weather modelers and high-end computing experts from five institutions to test whether representing mesoscale and sub-synoptic atmospheric processes in climate models improves climate simulation and prediction. For a part of Project Athena, numerical simulations were carried out with the European Centre for Medium-range Weather Forecasts (ECMWF) Integrated Forecast System (IFS), a hydrostatic spectral model used for operational forecasting. Multiple simulations with different resolutions were designed to increase weather and climate model resolution to accurately resolve synoptic and mesoscale atmospheric phenomena. The Athena supercomputer operated by the University of Tennessee's National Institute for Computational Science (NICS) and hosted by Oak Ridge National Laboratory (ORNL) was used as a dedicated computing resource to carry out these experiments. More details about Project Athena are provided in Kinter et al. (2013).

The IFS runs were done with four different horizontal resolutions, designated T159 (~126 km), T511 (~39 km), T1279 (~16 km), and T2047 (~10 km), respectively, where the resolution designation indicates the wave number of the triangular truncation of the spherical harmonic spectral expansion and the grid spacing is indicated in parentheses. Vertically, IFS is discretized with 91 hybrid levels (top full level at 0.01 hPa). The model includes a package of subscale physics parameterizations, which is state-of-the-art (Jung et al. 2012). There was no re-tuning of the parameters in the parameterization schemes for the different resolutions. Some parameterizations in IFS are scale-aware, e.g., the convective adjustment time in the deep convection scheme has a resolution-dependence that is largest for relatively low resolutions (i.e., from T159 to T511). By design, the parameterized orographic gravity wave drag is also reduced with increased horizontal resolution (Brown 2004).

Some of the IFS runs done in Project Athena are comprised of 13-month long integrations starting on 1 November of each of the years 1960–2007 for T159, T511, and T1279. The atmospheric initial conditions are from the 40-year ECMWF reanalysis (ERA-40) for the period of 1960–1989 and ERA-interim for 1990–2007, which are linearly interpolated to the corresponding model resolutions. All integrations were carried out with prescribed boundary conditions from observed SST and sea ice fields. In particular, the UK Met Office HADISST1 monthly mean fields were used for 1960–1981 (Rayner et al. 2003) and the weekly OISST-v2 for 1982–2001 (Reynolds et al. 2002). Both datasets are on a 1° latitude-longitude grid globally. For 2002–2008, daily SST from the operational ECMWF analysis is used (Jung et al. 2012).

Our analysis is based on the monthly mean output from the last 12 months of the integration after a 1-month spin-up. Most of the T511, T1279, and T2047 fields are truncated to T159 and interpolated to a corresponding N80 grid. Only a few selected fields, e.g., precipitation, are preserved on their native grids, corresponding to 320, 1024, 2560 and 4096 grid points along the equator for the four sets of runs, respectively. Using the truncated outputs, we can directly compare features at the same spatial scales from different model runs. Corresponding runs for T2047 were carried out only for the years 1989–2007. To maintain consistency across data sets, we have not included the T2047 runs in this analysis.

2.2 Minerva simulations

Since the Athena simulations described in Sect. 2.1 are atmospheric runs only, we have supplemented them with

a set of coupled model simulations from another research project to assess the effect of air-sea feedback. Project Minerva was a collaboration between the ECMWF and the Center for Ocean–Land–Atmosphere Studies (COLA) (e.g., Zhu 2015). In this project, a coupled model very similar to the ECMWF seasonal forecast system, version 4 (System 4), is used for seasonal hindcasts. The model includes an updated version of the IFS as its atmosphere component. The ocean component is the Nucleus for European Modeling of the Ocean (NEMO), version 3.0 (Madec 2008). Its horizontal configuration adopts the ORCA1 grid (http://www.noc.soton.ac.uk/nemo/), which has a horizontal resolution of approximately 1° (meridionally refined to 1°/3° near the equator). It has 42 levels in the vertical, 18 of which are in the upper 200 m. IFS and NEMO are coupled every 3 h.

In Project Minerva, three sets of seasonal hindcasts were performed with different atmospheric horizontal resolutions: T319 (~62 km), T639 (~31 km) and T1279 (~16 km), while the ocean resolution was fixed at a resolution comparable to that of the prescribed SST data in the Athena runs. The 7-month seasonal hindcasts of T319 (T639) with 51 (15) ensemble members were produced using the observed initial conditions of May 1 during 1980–2011 and November 1 during 1980–2010 (Zhu 2015). A subset (2000–2010 or 2011) of cases was run with the IFS at T1279 resolution. The ensemble initialization for both IFS and NEMO follows the same procedure as that for the operational ECMWF System 4 (Molteni et al. 2011). In this study, we use only the first 15 ensemble members for all three sets of hindcasts. The first month of integrations is discarded as spin-up.

2.3 CCSM3.5 simulations

Both the Athena and Minerva simulations examine the influence of the AGCM resolution at moderate oceanic resolution in either forcing or model. As we will show in Sect. 3, the oceanic setting plays an important role in these experiments. In order to further examine the impacts of oceanic fronts and mesoscale eddies, we also examined a pair of sensitivity simulations using a pre-release of NCAR Community Climate System Model (CCSM) version 4.0. The CCSM is a state-of-the-art coupled climate model consisting of atmosphere, ocean, land, and sea ice components. Details of the model configuration and an overview of the simulated climate for this set of experiments are given in Kirtman et al. (2012). Briefly, the atmosphere component is the Community Atmosphere Model (CAM) that uses the finite volume discretization (Lin and Rood 1997) and has 26 vertical levels in a hybrid coordinate. Its horizontal resolution is fixed at zonal grid spacing of 0.625° and meridional grid spacing of 0.5° in both experiments. The land component has the same horizontal resolution as the atmosphere component. The oceanic component has 42 levels vertically but different horizontal resolutions for the two runs, as discussed below. All the component models communicate via the CCSM flux coupler (Craig et al. 2011) where the fluxes at the air-sea interface are calculated at 6-h intervals using atmospheric state variables interpolated onto the ocean model grid and conservatively remapped onto the other component model native grids.

In this sensitivity experiment, the control run is a 155-year present-day climate simulation with CAM coupled to the oceanic and sea-ice components that have zonal resolution of 1.2° and meridional resolution varying from 0.27° at the equator to 0.54° in the mid-latitudes. The sensitivity run is carried out with the horizontal resolution of the oceanic and sea-ice component models increased to 0.1° in both latitude and longitude. In this case, the grid spacing is 11 km at the equator, gradually shrinking to 2.5 km in high latitudes, which fully resolves the mesoscale eddies in the ocean. The ocean model uses a biharmonic closure of horizontal mixing and diffusion for both momentum and tracers. The hyper-viscosity and diffusivity are resolution-dependent because they are scaled with the cube of the local grid spacing (Bryan et al. 2007). The initial conditions are the same for both the low and high-resolution simulations except that the ocean states are interpolated to their corresponding grids. For the high-resolution run, a filter is added to the polar winds to reduce computational instability after 102 years of spin-up. The experiment is then extended to 155 years. Kirtman et al. (2012) found that, although the polar filter produces some differences compared to the earlier part of the simulation, these differences are very small compared to those between the high-resolution and low-resolution simulations. In this study, we examine the climatology and seasonal cycle in the GS region using the last 53 years of the high-resolution simulation (after the polar filter is applied). The low and high-resolution runs will be referred to as LRC07 and HRC06 hereafter, following Kirtman et al. (2012).

2.4 Observational datasets

Several observational datasets are used for model verification in this study. The Tropical Rainfall Measurement Mission Project (TRMM) multi-satellite precipitation analysis (TMPA) daily rainfall estimate, version 7.0 (3B42 V7) covers global area from 50°S to 50°N with the spatial resolution of 0.25° latitude by 0.25° longitude (Huffman et al. 2010). Its period is from January 1998 to October 2012. Another observation dataset is the SLP and divergence on 23 pressure levels from ERA40 (Uppala et al. 2005), covering the period of September 1957 to August 2002. The ERA-40 data are originally on spectral format with the

resolution of T85 and have been transformed to a regular 2.5° latitude × 2.5° longitude grid for SLP and winds on pressure levels while the surface winds are at a Gaussian grid with 256 × 128 points globally.

The daily gridded SST fields using optimum interpolation (OI) analysis of the Advanced Very High Resolution Radiometer (AVHRR) is used in this study for coupled model SST verification (Reynolds et al. 2007). The OI-daily SST has a spatial grid resolution of 0.25° that matches the TMPA precipitation in both spatial and temporal resolution and also has a better representation of the SST front and mesoscale features in the Gulf Stream region. Both Pathfinder (from January 1985 to December 2005) and operational AVHRR data (2006 onward) are blended with in situ SST measurements from ships and buoys, with a large-scale adjustment of satellite biases with respect to the in situ data.

3 Precipitation climatology in the Gulf Stream region

This section investigates the impacts of horizontal resolution on precipitation climatology in the Gulf Stream region. First, we focus on the Athena simulations with different IFS resolutions, forced by prescribed SST from the observations. Then the effects of air-sea coupling will be further examined using the coupled runs.

3.1 The Athena simulations

Figure 1 displays the annual climatological precipitation (shaded) in the Gulf Stream region from the TMPA observations (Fig. 1a) and the IFS simulations (Fig. 1b–f), with the observed annual SST climatologies (contour) overlaid. The SST field superimposed in TMPA precipitation (Fig. 1a) is from OI-daily, while the SST overlaid in the remaining panels are from the corresponding prescribed SST in each of the IFS simulations. For simulations at T511 and T1279, the mean precipitation is plotted on the respective native grids (left panels) and on the grid with the spectrum truncated at T159 (right panels) equivalent to that of the lowest resolution run (Fig. 1b). The averaged precipitation of the Athena simulations is for the period 1998–2008, consistent with the period of the high-resolution TMPA observations. We have also examined the climatologies of the Athena model precipitation for the whole period of 1960–2008 and the period of 1982–2008 forced with the weekly OISST. Although the characteristics of the model differences are qualitatively similar among the three periods, the qualitative difference is largest in the last period (1998–2008). This is possibly because the SST boundary condition since 2002 is the higher-resolution Real-Time Global (RTG) analyses of 0.5° × 0.5° grid (Thiébaux et al. 2003). Previous studies have shown that the RTG SST forcing generates stronger atmospheric responses in the operational ECMWF numerical weather prediction model (e.g., Chelton 2005; Song et al. 2009).

The TMPA observations (Fig. 1a) show a narrow band of strong precipitation over the North Atlantic Ocean closely related to the sharp SST gradient, the oceanic front associated with the Gulf Stream and its extension. This rain band (>5 mm/day, green shading) extends from the southwest Florida Coast to the Gulf Stream (GS) extension, and then turns northeastward with the North Atlantic Current (NAC). The strongest precipitation is located at the southern edge of the SST front where the water temperature is higher. The largest rainfall occurs near and to the south of the 20 °C isotherm of SST, and the strong rain belt of intensity higher than 7 mm/day closely follows the SST isotherm starting from the east coast of Florida at about 30°N, extending first northeastward along the coast, then more eastward to 40°N and close to 50°W (yellow shading). Within this rain belt, there are localized centers of rainfall exceeding 8 mm/day (orange shading).

All the IFS simulations in the remaining panels reproduce these characteristics qualitatively although they underestimate the precipitation intensity of this rain band compared to the TMPA (Fig. 1a). The T159 simulation is the weakest. Its main area of precipitation over 5 mm/day is confined within the GS extension region between 50°W and 70°W, which is weakened significantly close to the coast between 20°N and 30°N and further northeastward (Fig. 1b). The southwestern branch never reaches the rainfall level of 6 mm/day. Over the NAC area, only a small area is about 5 mm/day, which is detached from those further to the southwest. In addition, the main precipitation region in 50°–70° is also narrower meridionally than the observed because its northern edge retreats southward. As the IFS resolution increases, the simulated mean precipitation tends to increase along the track of the GS extension and NAC and agrees more closely to the observations. The T511 run (Fig. 1c, d) shows significant rainfall enhancement over that of the T159 run throughout the GS region as measured by the expansion of the area with precipitation over 5 mm/day. In the northeast, this area extends further north than the observed one. The rain band also extends its southern end southward along the coast to be more consistent with the observations. At the center, the rain band expands meridionally with maximum intensity increasing to over 7 mm/day. The highest resolution (T1279) run (Fig. 1e, f) shows further enhancement in all of these aspects and yields the best pattern and magnitude of the primary precipitation centers. In particular, a clearly defined maximum appears over the NAC at around 42°N and 45°W to represent the secondary center on the NAC track more realistically.

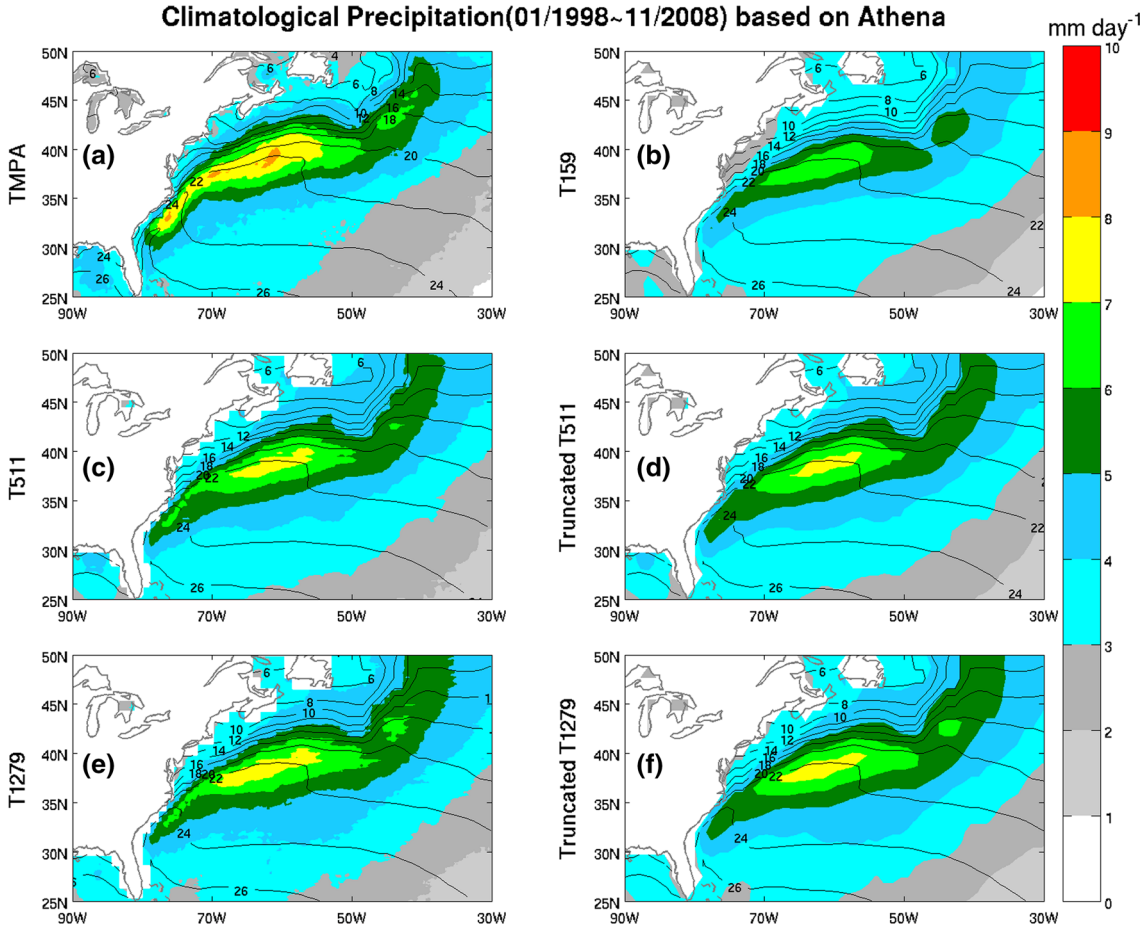

Fig. 1 Annual precipitation climatology (unit: mm day^{-1}; *shaded*) in the Gulf Stream region (25°N–50°N, 30°W–90°W) from TMPA observations and Athena IFS simulations for 01/1998–11/2008. The superimposed contours are the observed SST climatology (°C) for the same period from the OI-daily observations and the SST climatologies in model simulation panels from their corresponding run outputs. **a** Shows the observed mean rainfall derived from TMPA monthly precipitation. The IFS mean precipitation are averaged from the last 12 months of the 13 month hindcast runs initialized at 12 Z, November 1 for each year from 01/1998–11/2008, approximately 12 hindcasts in total are averaged to form the mean state. The IFS hindcasts are conducted with different resolutions from T159 (**b**), T511 (**d**) and T1279 (**f**). The model outputs in these *three panels* are presented on the same grid network, with the T511 and T1279 output truncated to the Gaussian grid T159. The T511 and T1279 output on their native grids are shown in (**c**) and (**e**), respectively

For both T511 and T1279 runs, the precipitation bands from the native grids (Fig. 1c, e) are similar in pattern to the truncated versions (Fig. 1d, f) and there is a slight improvement in the intensity. This suggests that the improvements generated by increased model horizontal resolution occur mostly on relatively large scales. As a result, the data truncation serves primarily as a smoother in the simulated precipitation. However, the precipitation on native grids has a narrow band of enhancement in the southwest over 6 mm/day in both T511 and T1279 that has been smoothed out by the truncation.

The improvements of the GS precipitation with higher model resolution can also be seen seasonally. Figure 2 shows the seasonal climatology of the observed and simulated precipitation. The climatological means of the GS seasonal precipitation are presented from the top to bottom rows for the boreal winter (December–February, DJF), spring (March–May, MAM), summer (June–August, JJA) and autumn (September–November, SON) respectively. Within each row, the four panels show the corresponding seasonal precipitations (shading) and SST (contours) for TMPA, T159, T511 and T1279 from left to right. The TMPA observations show two distinctive precipitation patterns over the Gulf Stream region in DJF (Fig. 2a) and JJA (Fig. 2c), featuring strong precipitation over the GS extension and NAC track in the former while over the Florida Current and western GS in the latter. The seasonal transitions occur in MAM (Fig. 2b) and SON (Fig. 2d). The seasonal change is associated with a transition of rainfall regimes, with an SST gradient-driven convergence within the marine boundary layer over the GS extension and the NAC track but a convective heating over warm water of the

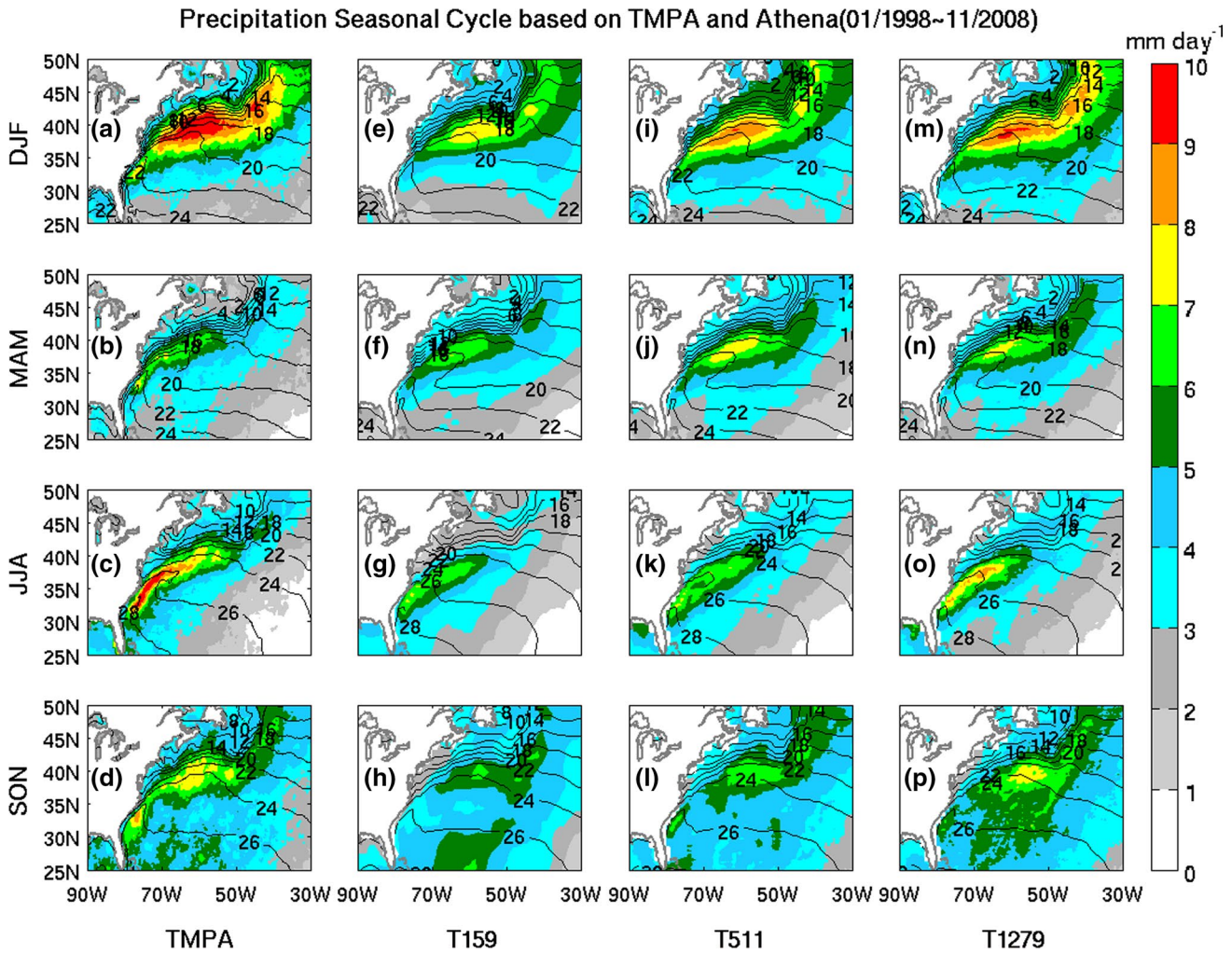

Fig. 2 Seasonal precipitation climatology (*shading*) of TMPA and Athena simulations with the seasonal SST climatology (°C; *contours*) from observed OI-daily (for TMPA) and the corresponding runs (for Athena) overlaid on each *panel*. The *color bar* of precipitation (unit: mm day^{-1}) is on the *right*. The contour interval is 2 °C. Within *each row*, the *panels* are organized as TMPA, T159, T511 and T1279 from *left* to *right*, and within each *column*, the seasonal means of DJF, MAM, JJA and SON are from *top* to *bottom*

Florida Current and western GS (Minobe et al. 2010). More detailed discussions are given below for each of the four seasons.

The pattern of the observed DJF precipitation is similar to that of the annual mean (Fig. 1a), with a main center along the GS extension between 50°W and 70°W and a secondary one on the NAC track around 40°W. The precipitation, however, is much stronger than the annual mean (over 10 mm/day in both centers) and with a broader range across the oceanic front. All resolution simulations (Fig. 2e, i, m) capture these general characteristics but underestimate the rainfall intensity. In particular, the lowest resolution run (T159) has the weakest rainfall and largely fails to reproduce the NAC center (Fig. 2e). The resolution increases enhance the rain band and expend its range, as seen by the widening edges of the 7 mm/day shading. The T1279 run (Fig. 2m) is closest to the observed.

By MAM, the observed GS precipitation (Fig. 2b) is weakened dramatically to around 6–7 mm/day in maxima. The rain belt (>5 mm/day, green shading) also shrinks southwestward, to be confined over the warm waters of the Florida Current and western GS. As a result, the NAC center vanishes and the main rain belt is narrowed. The simulations (Fig. 3f, j, n), though showing a reduction of precipitation from DJF, maintain an excessively strong and broad rain band with a center over the GS extension. The area of large rainfall (>5 mm/day) also extends too far north along the NAC track. Overall, the model rainfall pattern in spring is similar to that in winter, lacking a clear seasonal transition in runs of all resolutions. Curiously, the

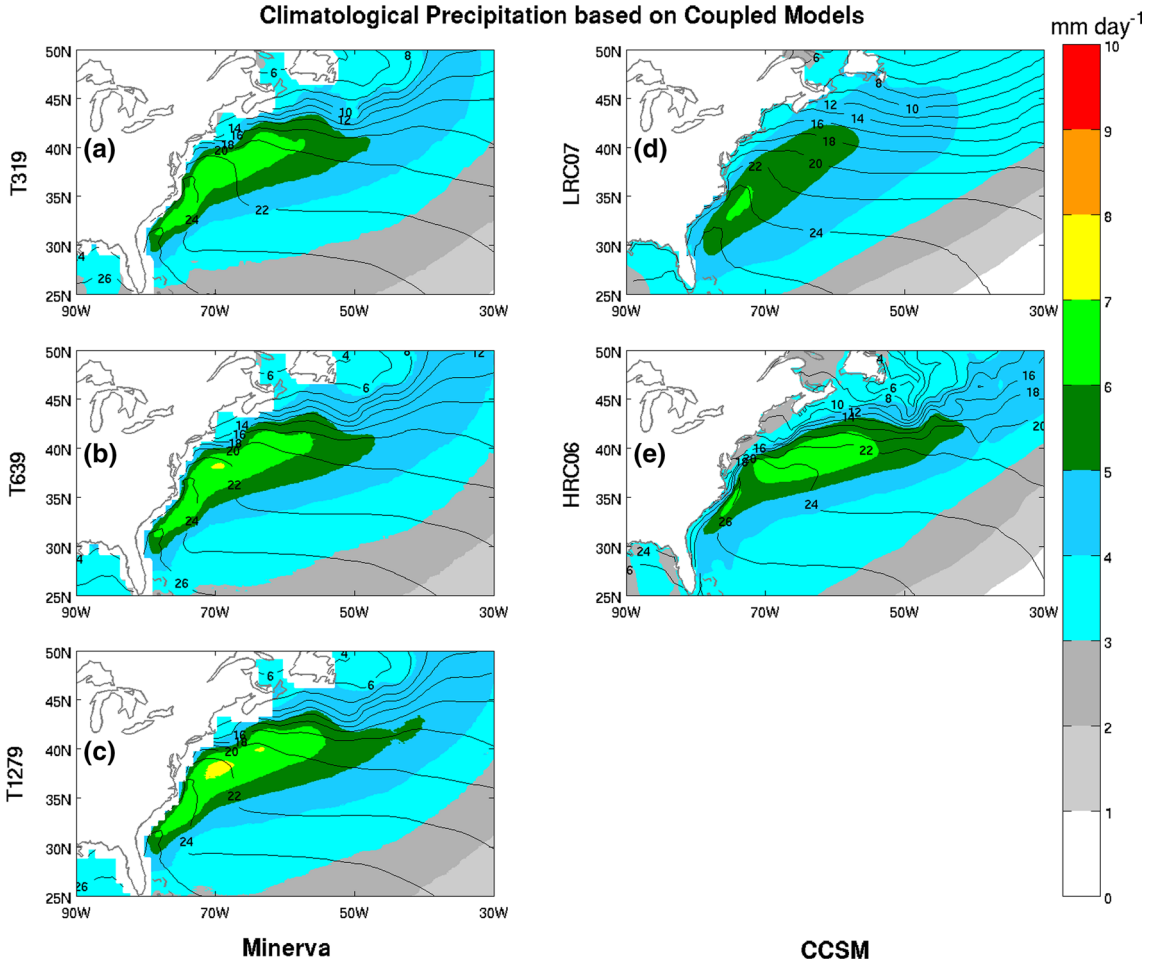

Fig. 3 The Climatological annual mean precipitation (*shading*) and SST (*contour*) from the Minerva hindcasts for 1980–2011 (*left column*) and CCSM3.5 (*right column*). Within the *left* (*right*) *column*, the *panels* from *top downward* correspond to the increasing atmospheric (oceanic) resolutions. The contour interval is 2 °C and the *shading* scale is shown on the *right*

precipitation center is stronger at T511 (Fig. 2j) than those at lower (Fig. 2f) or higher resolutions (Fig. 2n).

In JJA, the observed summer precipitation (Fig. 2c) has largely the same pattern as that of MAM but the mean precipitation is significantly intensified over the Florida Current and western GS, possibly because the underlying SST is much warmer. By this season, the IFS simulations have also completed the seasonal transition to the summer pattern, with weakened rainfall over the NAC and shifted main rain belt to the Florida Current and western GS, although all models underestimate the precipitation there (Fig. 2g, k, o). The T1279 model simulates the JJA precipitation most realistically (Fig. 2o).

In SON, the observed precipitation centers on the GS extension and the NAC track are re-established while the rainfalls over the Florida Current are weakened (Fig. 2d). As a result, the mean precipitation in SON highlights a northward shift toward the DJF rainfall pattern. Furthermore, there is a general increase of precipitation over a broader area of the North Atlantic, as shown by the expansion of precipitation over 3–4 mm/day (blue shadings). The simulations (Fig. 2h, l, p) reproduce this seasonal transition well, including the shifting of the GS precipitation center and broadening of rainfall area over the North Atlantic. Again, the T1279 run produces the most realistic precipitation in the GS extension and NAC track (Fig. 2p). This run, however, overestimates the precipitation in the subtropical Atlantic between 30°N and 35°N.

Overall, the IFS produces a realistic seasonal cycle of the precipitation. The major shortcomings are that the seasonal transition in boreal spring seems to be significantly delayed in all resolution runs and the overall intensity of rainfall is underestimated although the resolution increases do improve the latter. In particular, the IFS simulation with 16-km resolution is best in both the magnitude and meridional range of the precipitation over both the Florida Current and the GS extension. It also improves the precipitation over the NAC track significantly.

3.2 The effects of air–sea coupling

We further examine the effects of air–sea coupling on the simulated GS precipitation. Figure 3 shows the climatological annual mean precipitation (shading) and SST (contour) from the Minerva hindcasts for 1980–2011 (left column) and CCSM3.5 (right column). For Minerva, the annual climatology is averaged from both the summer and winter hindcasts. Comparing the Athena simulations (Fig. 1) with their Minerva counterparts (left column, Fig. 3), it is clear that the air–sea coupling generally weakens the GS precipitation and also shifts its center southwestward, with enhanced precipitation over the Florida Current and western GS but weakened precipitation over the GS extension. An increase of the IFS resolution from 62 km (Fig. 3a) to 16 km (Fig. 3c) enhances the center of precipitation modestly. None of the simulations reproduces the secondary center on the NAC track. Similar features are also shown in the LRC run (Fig. 3d) of CCSM3.5, where the mean precipitation is weaker and its center (>6 mm/day) is shifted further west and oriented along the coast.

These characteristics of coupled simulations can largely be explained by the deficiencies of the simulated SST climatology near the oceanic front by the non-eddy-resolving OGCMs. In the Minerva runs, the oceanic front is located at 40°N–45°N (left panels, Fig. 3), further to the north of the observed one (Fig. 1a). This is because of an overshoot of the western boundary current separation latitude, which is common in non-eddy-resolving ocean models (e.g., Kiehl and Gent 2004). Moreover, the path of the GS extension and NAC is too zonal after the separation point near the Grand Banks. Correspondingly, a large area of cold SST bias (Fig. 4a), up to 4 °C at its center near 45°N–50°N and 40°W–50°W, extends from the northeastern North Atlantic toward the American coast near 30°N, which surrounds a substantial warm bias at the coastal region between 35°N and 45°N. This error pattern is not sensitive to the increase of the IFS resolution because the mean SST differences between these runs (Fig. 4b, c) are

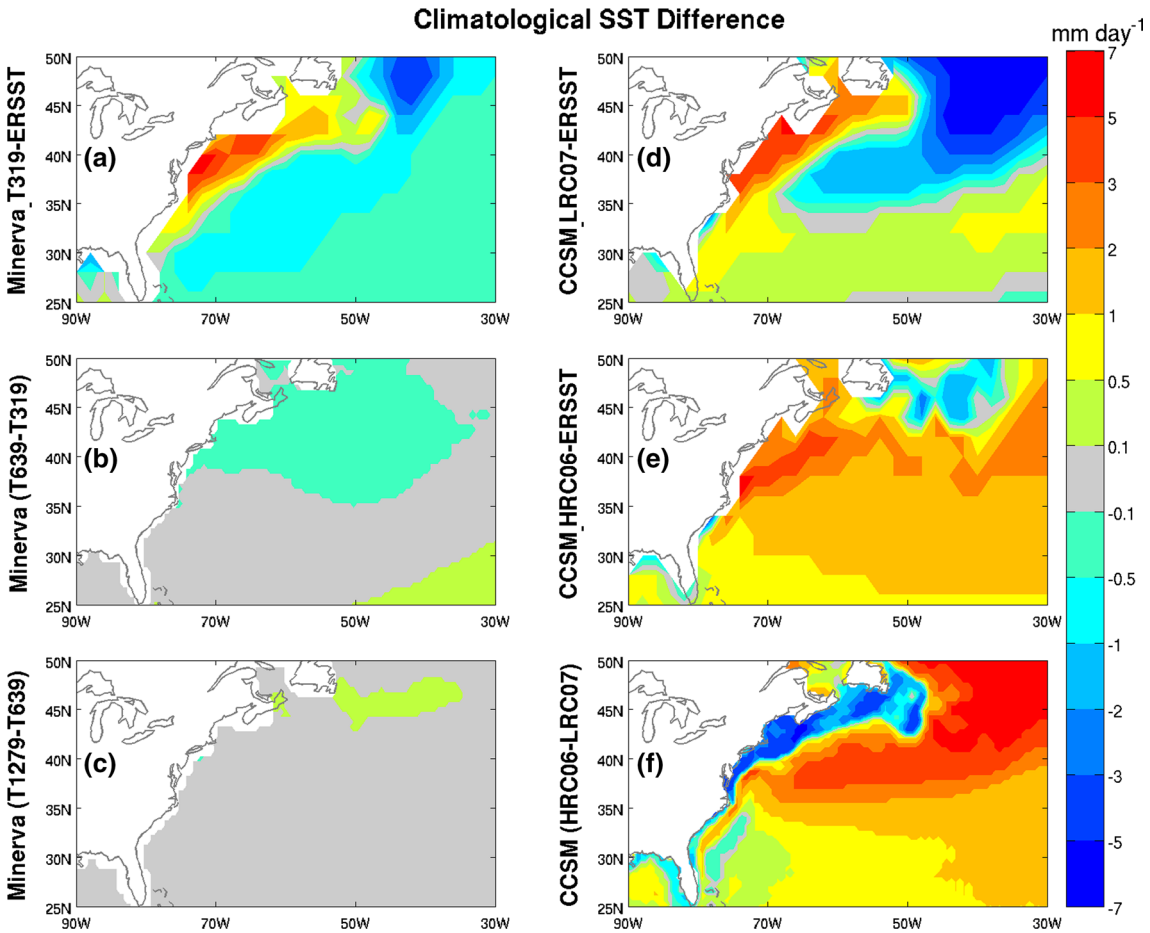

Fig. 4 **a** Mean SST error of Minerva T319 runs. **b** Mean SST difference between Minerva T639 and T319 (T639–T319), and **c** difference between Minerva T1279 and T639 (T1279–T639). **d** Mean SST error of CCSM LRC07, and **e** CCSM HRC06. **f** Mean SST difference between CCSM HRC06 and LRC07 (HRC06–LRC07)

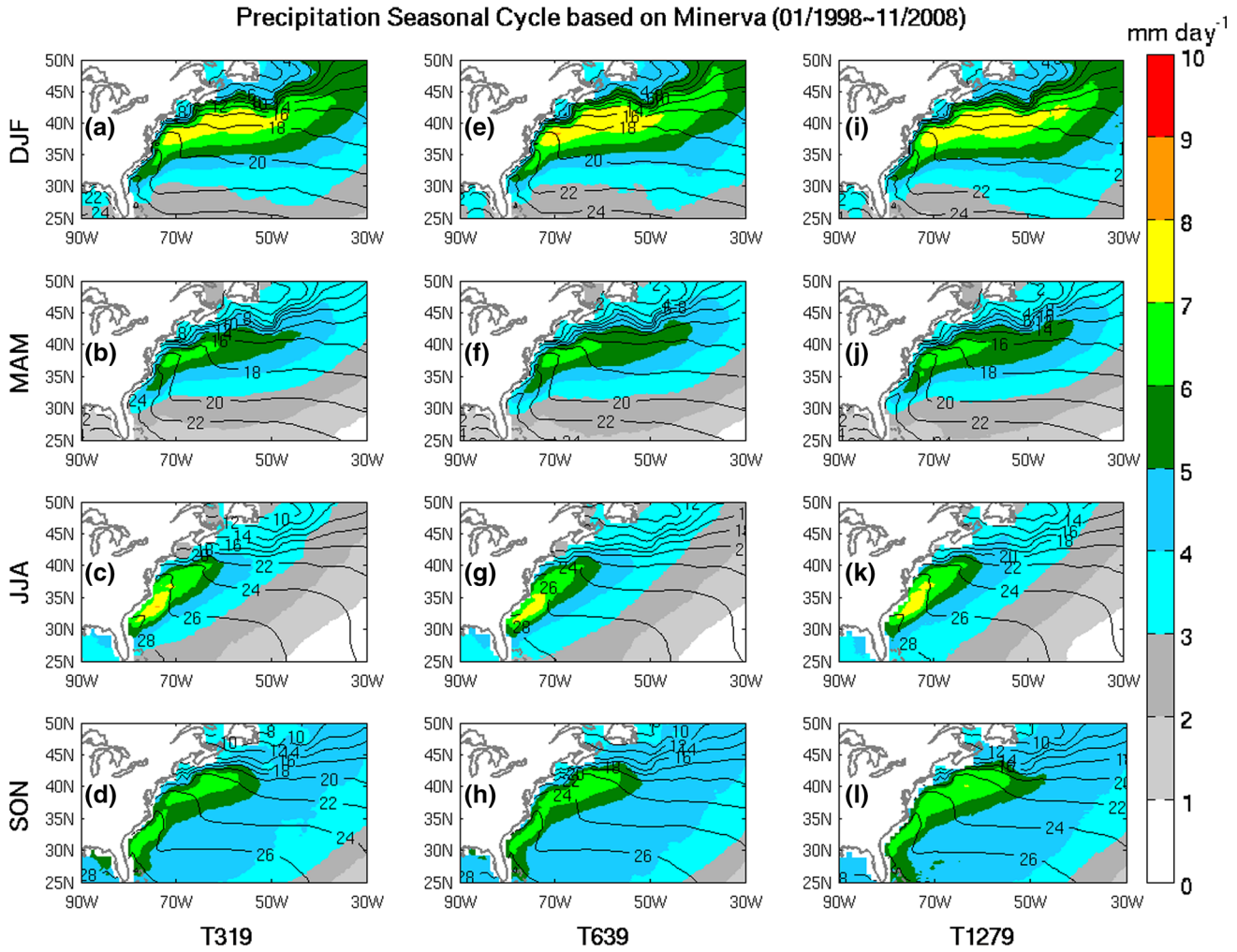

Fig. 5 Seasonal precipitation climatology (*shading*) of Minerva simulations at the resolutions of T319 (*left panels*), T639 (*middle panels*) and T1279 (*right panels*). The *color bar* of precipitation (unit: mm day^{-1}) is on the *right*. The seasonal SST climatology (°C; *contours*) from the corresponding runs is overlaid on each *panel*. The contour interval is 2 °C. Within each column, the seasonal means of DJF, MAM, JJA and SON are organized from *top* to *bottom*

much smaller than their SST errors (not shown), which are very similar to that shown in Fig. 4a. As a result, the oceanic frontal precipitation is substantially weakened.

The SST errors of the LRC run (Fig. 4d) have a similar pattern to that of the IFS simulations but with even larger magnitude because its SST front is more diffuse (contour, Fig. 3d). However, as the OGCM resolution of the CCSM3.5 is increased to 0.1°, the SST gradient of the HRC06 run is tightened significantly near 40°N (contour, Fig. 3e). The high-resolution OGCM depicts the oceanic front and jet more accurately although it seems still too zonal. The separation point of the western boundary current is closer to the observed because the more realistic partitioning of the mean and eddy energy levels reduces its dependence of lateral friction (e.g., Chassignet and Marshall 2008). Correspondingly, the HRC06 precipitation is improved significantly from the LRC run, as pointed out by Kirtman et al. (2012). The center of precipitation is oriented more zonally and aligned with the oceanic front. Its magnitude is also enhanced substantially.

Both the Minerva and CCSM simulations reproduce the annual cycle of the GS precipitation realistically (Figs. 5, 6). In both sets of runs, there is a clear intensification of the mid-latitude rainfall over the GS extension and its westward expansion from SON to DJF. The enhancement of the rainfall over the Florida Current is also well simulated. The seasonal transition from winter to summer seems better handled by the coupled models than uncoupled ones with a clearer weakening of precipitation and westward withdraw in the former. The fall broadening of the precipitation over the North Atlantic is also simulated realistically. In the Minerva runs, the effect

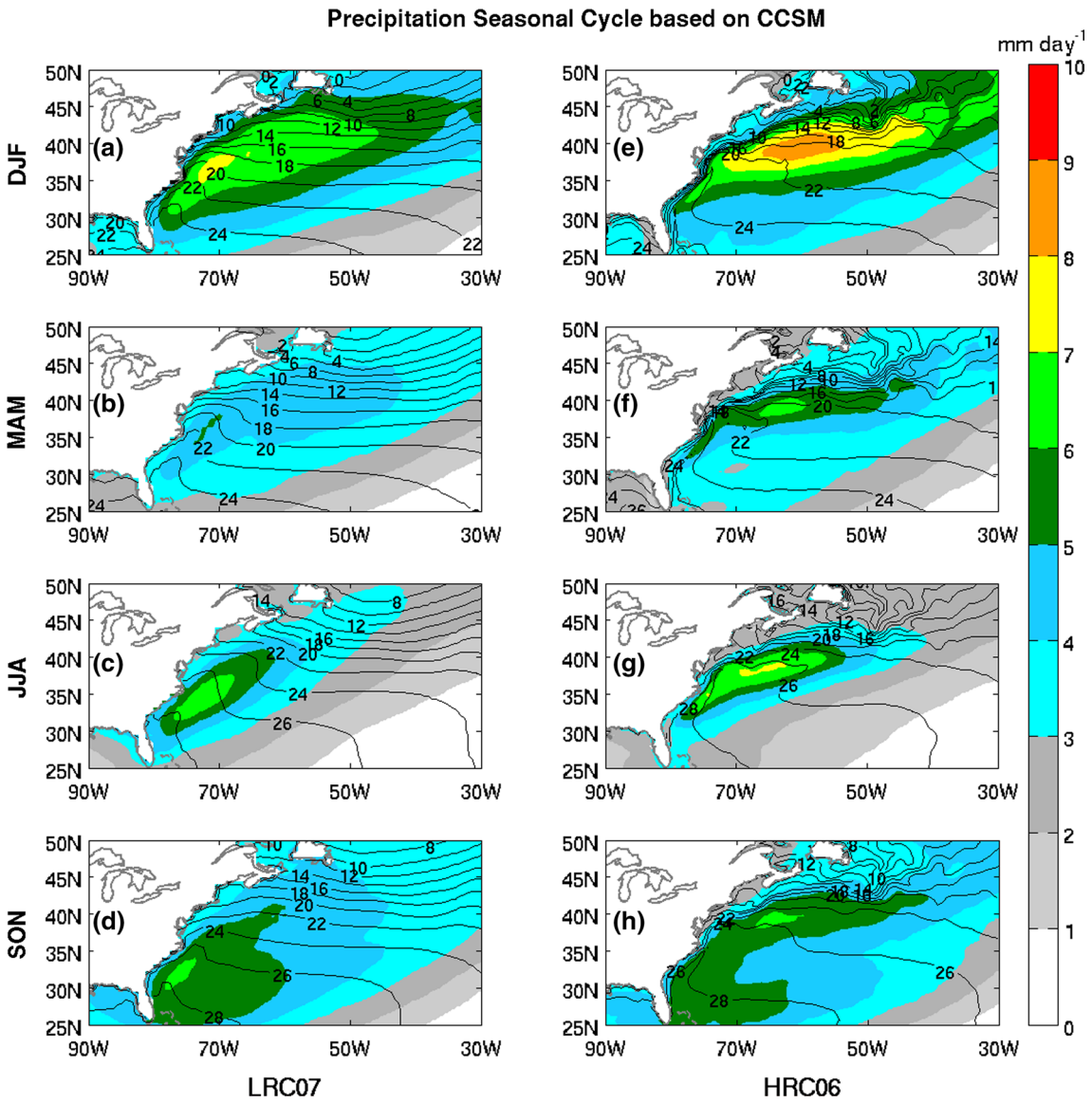

Fig. 6 Seasonal precipitation climatology (unit: mm day^{-1}; *shaded*) from CCSM3.5 LRC07 and HRC06 coupled model simulations. The model corresponding seasonal SST climatologies are superimposed as contours on the corresponding *panels*. The contour interval is 2 °C. The seasonal means for DJF, MAM, JJA and SON are organized from *top* to *bottom panels* and LRC07 and HRC06 runs are in the *left* and *right panels*, respectively

of the increased IFS resolution is a quantitative intensification of precipitation in all seasons (Fig. 5). On the other hand, the improvement in the HRC06 simulation is qualitative, with a much more realistic annual cycle than the LRC run (Fig. 6). As in the annual mean, the annual cycle in the latter is dominated by the changes over the warm water in the western boundary, with an excessive weakening in MAM. The former, however, shows a clear seasonal transition between the dominant precipitation over the boundary and GS extension.

The above analysis of the three sets of experiments shows that, forced with observed SST, atmospheric models can produce the main characteristics of the rain band over the Gulf Stream region associated with the SST front even at moderate model resolutions. A resolution increase is able to improve the quality of the model simulations in several aspects, especially over the GS extension and the NAC track, simply because the underlying SST gradient can be better "seen" by the atmosphere. The coupled model simulations fail to reproduce the secondary precipitation center and generally weaken the overall precipitation in the GS region. However, the eddy-resolving ocean model produces qualitative improvements of the SST simulation.

4 Potential mechanisms

One potential mechanism for stronger GS precipitation with increased atmospheric and/or oceanic model resolutions is that the storm track is enhanced in the higher-resolution models. However, our examination of the storm track intensity based on dynamical variables (Wettstein and Wallace 2010) does not provide clear evidence to support this scenario. A separate analysis that a student intern has been doing (Kinter, personal communication) confirms that the North Atlantic storm track simulation in DJF is essentially insensitive to atmospheric model resolution in the Minerva hindcasts from November initial conditions. Following the framework provided by Minobe et al. (2008), we have also explored whether the mean atmospheric adjustment to the SST gradient plays a role. Using the Lindzen and Nigam (1987) marine boundary layer model, Minobe et al. (2008) showed that the Laplacian of the atmospheric sea level pressure ($\nabla^2 SLP$) forces the near-surface convergence $-(u_x + v_y)$:

$$-\rho_o\left(u_x + v_y\right) = \frac{\in}{\in^2 + f^2}\nabla^2 SLP \tag{1}$$

where ρ_o is the surface air density, $\in$ a constant damping coefficient and f the Coriolis parameter. Minobe et al. (2008) further pointed out that $\nabla^2 SLP$ itself is roughly proportional to the Laplacian of the SST with the sign reversed ($-\nabla^2 SST$) where the Laplace operator acts as a high-pass filter to separate the boundary layer SLP adjustment forced by the SST gradient from other larger-scale atmospheric variations. They also argue that this forced near-surface convergence generates vertical motion above the marine boundary layer and causes divergence in the mid-to-upper troposphere. In the following subsections, we first examine the pattern of the annual mean precipitation, which is representative of the fall and winter precipitation. The summer precipitation is then analyzed separately because it has some unique features.

4.1 Annual mean pattern

Figure 7 displays the climatological surface convergence in the Gulf Stream region (Fig. 7a), the negative Laplacian of the SST (Fig. 7b), the upper level divergence (Fig. 7c) and the Laplacian of the SLP (Fig. 7d) from the ERA-Interim reanalysis, all shown with the climatological SST overlaid

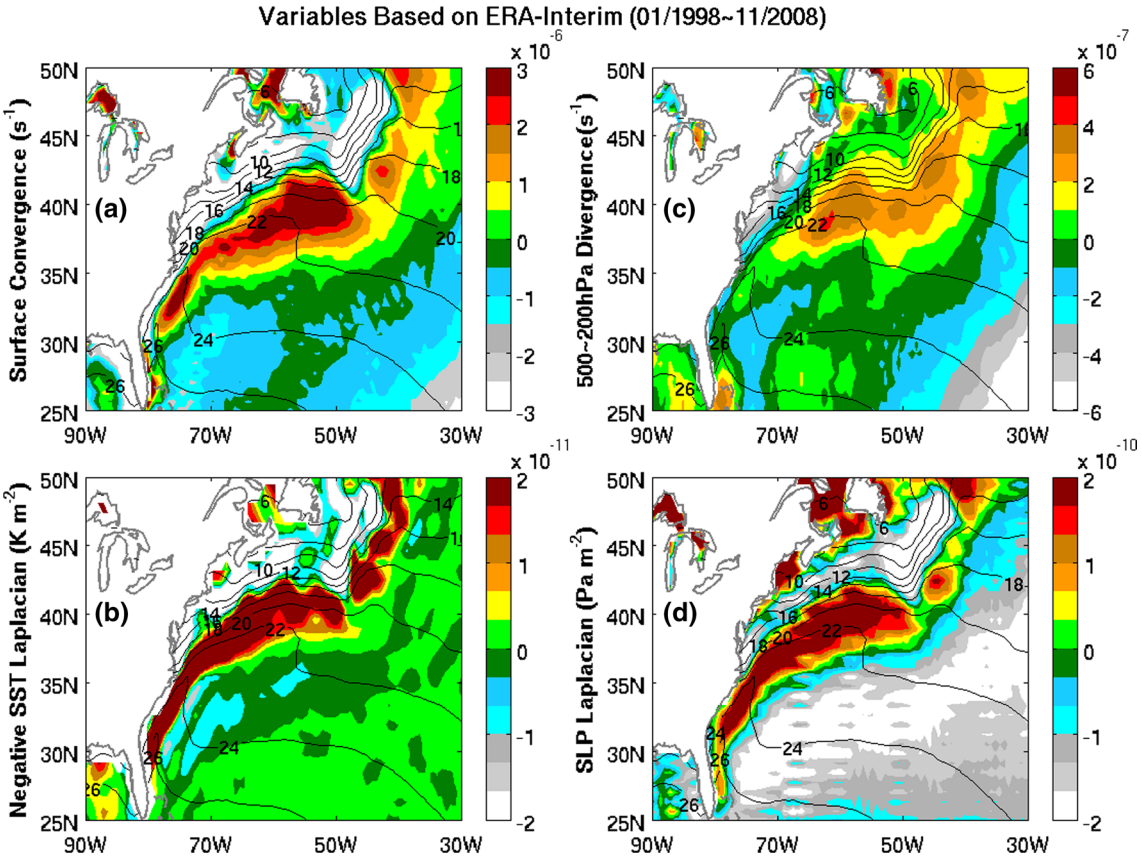

Fig. 7 *Shadings*: climatologies of **a** surface convergence (unit: s^{-1}), **b** negative laplacian of SST (unit: °C m^{-2}), **c** 500–200 hPa divergence (unit: s^{-1}) and **d** SLP laplacian (unit: Pa m^{-2}) based on ERA-Interim. The corresponding *color bar* is on the *right* of each *panel*. The SST climatology (°C) from ERA-Interim is overlaid as contours in each *panel*. The contour interval is 2 °C

(contours). The patterns of $\nabla^2 SLP$ (Fig. 7d) and $-\nabla^2 SST$ (Fig. 7b) are similar to each other with maxima over the southern edge of the SST gradient. Consistent with Eq. (1), the maxima of the SLP Laplacian overlap with those of the surface wind convergence (Fig. 7a), which also coincide with the location of the TMPA observed rain. Furthermore, the upper-level divergence has a maximum in the same area (Fig. 7c), suggesting that relatively deep circulation is invoked. This relationship confirms Minobe et al.'s (2008) results that the pressure adjustment to sharp SST gradients causes surface wind convergence, which induces ascending motion in the troposphere and divergence in the upper atmosphere.

Figure 8 displays the same variables as in Fig. 7, except that they are from the Athena simulation at T159 resolution. In order to remove the noise influence, a 9-point smoothing is applied to the fields of the SST and SLP Laplacian of the model outputs. It is clear that the model reproduces the observed processes qualitatively, although the response of the SLP Laplacian near the SST front is weaker (Fig. 8d). We have also examined these quantities from other Athena runs with higher resolution (not shown). They show the same quantities as those in Fig. 8.

The left panels of Fig. 9 further show the differences of divergence/convergence between the two runs (T1279–T159) in the upper (Fig. 9a) and lower (Fig. 9b) atmosphere, as well as the difference of SLP Laplacian (Fig. 9c). These figures suggest that the SST gradient-induced convergence process is enhanced modestly as the model horizontal resolution increases. Furthermore, decomposing the difference of total precipitation between the two runs (Fig. 9d) into its convective (Fig. 9e) and stratiform (Fig. 9f) components, it can be seen that the spatial patterns of the Laplacian of SLP (Fig. 9c) and stratiform precipitation (Fig. 9f) are similar to each other, with a general broadening toward the warm side of the SST gradient. On the other hand, the upper atmospheric divergence (Fig. 9a) and the convective precipitation (Fig. 9e) are more similar to each other, with the convective rain belt narrowly confined in a zone of the high SST gradient. This suggests that only the portion of the enhanced surface convergence near

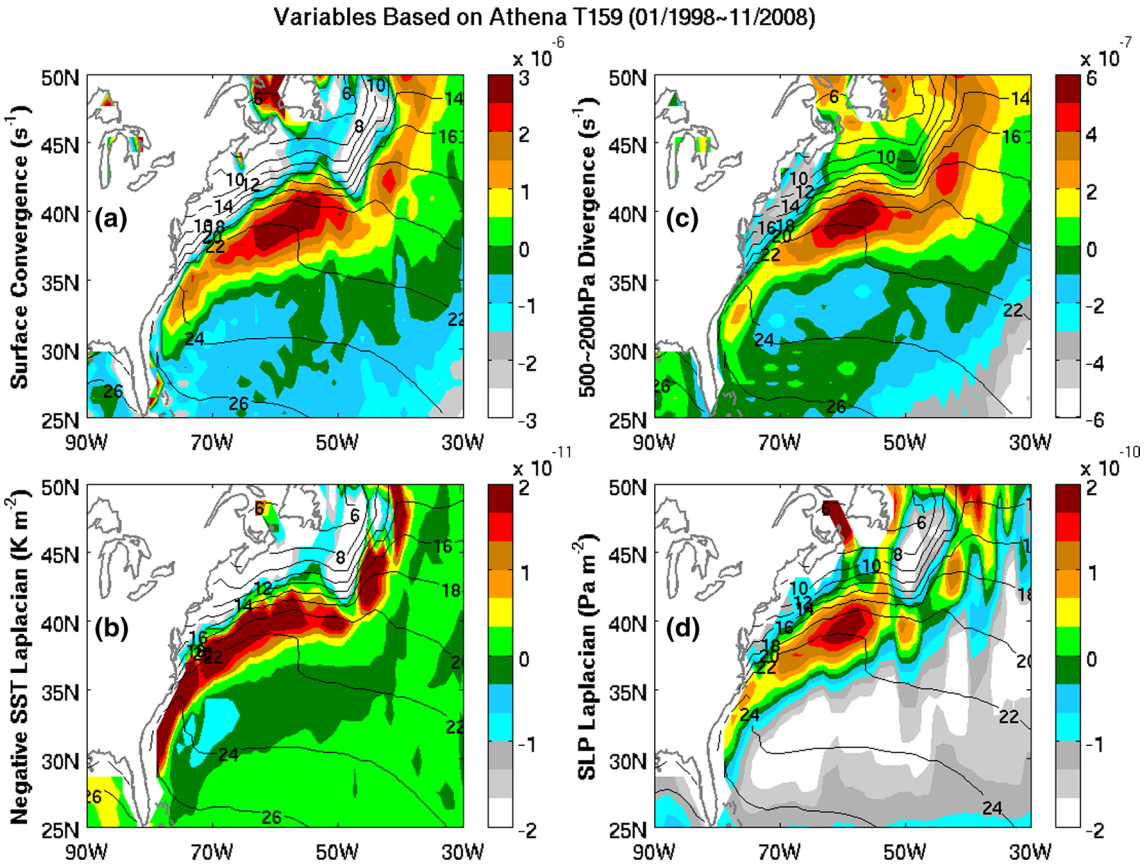

Fig. 8 *Shadings*: climatologies of **a** surface convergence (unit: s^{-1}), **b** negative laplacian of SST (°C m^{-2}), **c** 500–200 hPa divergence (unit: s^{-1}) and **d** SLP laplacian (Unit: Pa m^{-2}) based on Athena T159. The corresponding *color bar* is on the *right* of each *panel*. The SST climatology (°C) from T159 is overlaid by contours in each *panel*. The contour interval is 2 °C

the oceanic front contributes to the deep convection and affects the circulation in the upper troposphere. It should be noted that, since the wind and SLP output from the higher-resolution model runs have been truncated to T159, the contribution of the smaller-scale atmospheric fluctuations is not included in these calculations. It is still possible that some precipitation change is generated by the smaller-scale processes directly.

The Minerva simulations demonstrated somewhat similar features to those of Athena (not shown). This is mainly because the responses of the non-eddy-resolving OGCM to the AGCM with different resolutions are very similar. As discussed in the preceding section, the differences of the mean SST in the Minerva T319 run, compared with the T639 (Fig. 4b) and T1279 (Fig. 4c) runs, are less then 0.5 °C. On the other hand, the OGCM resolution increase in the CCSM3.5 runs generates much more dramatic changes in the mean SST. As the OGCM resolution is increased to eddy-resolving, however, the mean SST front in HRC06 is sharper than those from the observations (Fig. 4e). As a result, the pattern of mean SST difference between HRC06 and LRC07 (Fig. 4f) is reversed compared to Fig. 4d.

This mean SST difference may explain the substantially different atmospheric patterns between the LRC07 and HRC06 simulations. Figure 10 shows that, associated with the weak SST front in LRC07, strong surface convergence (Fig. 10a), as well as the Laplacians of both SST (Fig. 10b) and SLP (Fig. 10d), is limited to the coastal regions, away from the GS extension. Furthermore, in the upper level, there is a broad pattern of divergence (Fig. 10c) with its center over the warmest water in the southwest, which is quite different from the narrow convergence belt in the boundary layer (Fig. 10a). This implies that the upper level divergence, i.e., the deep convection, in this region is not mainly forced by the SST gradient induced surface convergence. This point will be further illustrated in the next subsection. In HRC06, however, the patterns in the atmospheric boundary layer and the upper levels are much more consistent with each other (Fig. 11). The center of action

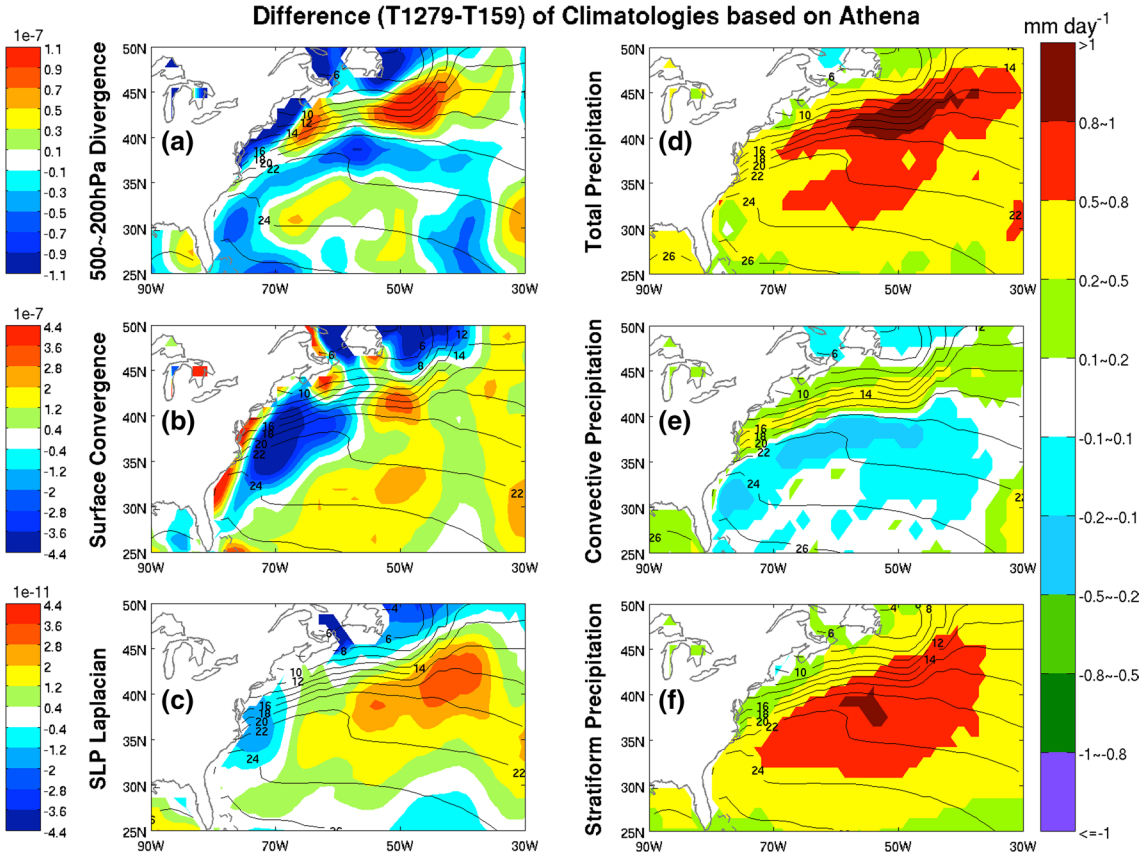

Fig. 9 *Shadings*: Climatological differences (Athena T1279–T159) of **a** 500–200 hPa divergence (unit: s^{-1}), **b** surface convergence (unit: s^{-1}), **c** the SLP laplacian (unit: Pa m^{-2}), **d** total precipitation, **e** convective precipitation and **f** stratiform precipitation. The unit of precipitation is (unit: mm day^{-1}). The corresponding *color bar* is on the *right* of each *panel*. The SST climatology (°C) from T159 is overlaid as contours in each panel. The contour interval is 2 °C

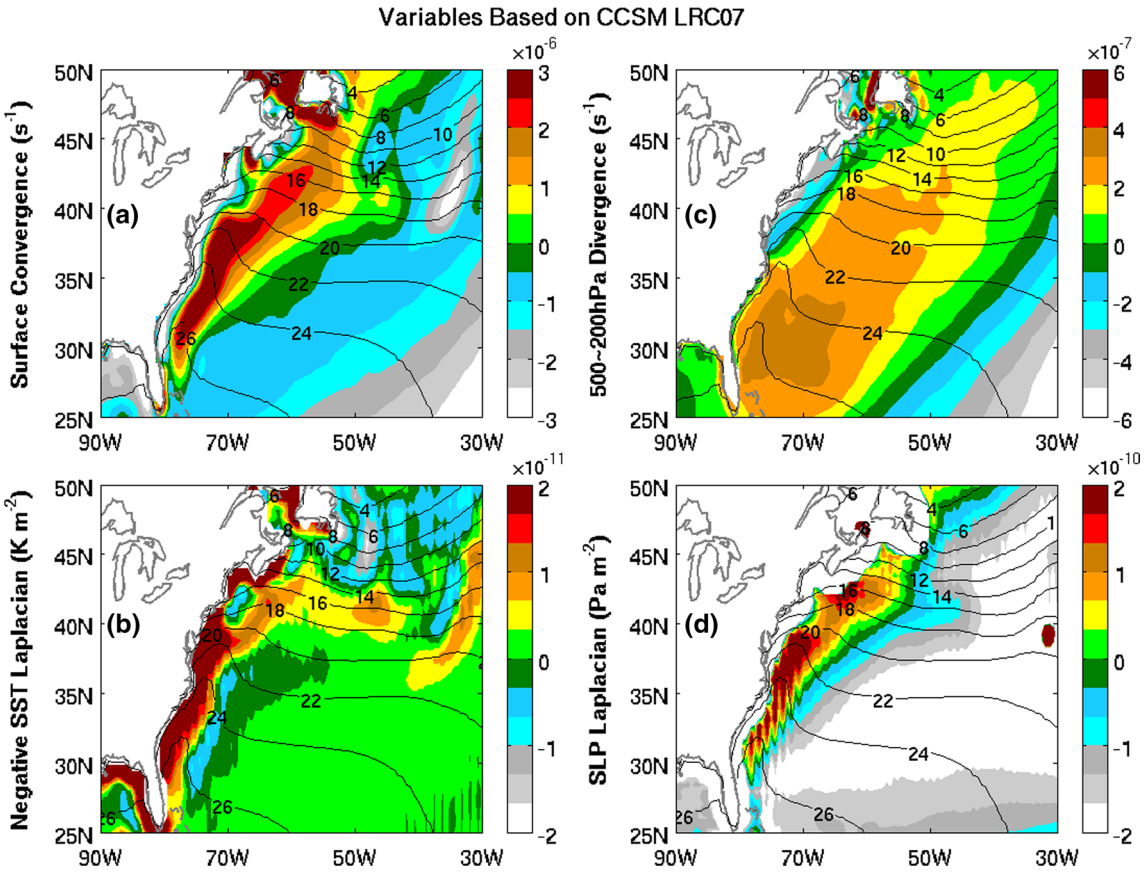

Fig. 10 *Shadings*: climatology of **a** surface convergence (unit: s^{-1}), **b** negative laplacian of SST (unit: °C m^{-2}), **c** 500–200 hPa divergence (unit: s^{-1}) and **d** the SLP laplacian (unit: Pa m^{-2}) based on CCSM3.5 LRC07. The corresponding *color bar* is on the *right* of each *panel*. The model SST climatology (°C) is overlaid as contours in each *panel*. The contour interval is 2 °C

is also shifted to the GS extension where the SST gradient is strongest. Compared with LRC07, the increase of the total precipitation in the GS extension (shading, Fig. 12a) over the enhanced SST gradient there (contour, Fig. 12a) is predominantly due to the convective precipitation (shading, Fig. 12d). This increase is closely associated with the enhanced Laplacians of the SLP (Fig. 12b) and SST (Fig. 12e). Moreover, the enhanced surface convergence (shading, Fig. 12c) and divergence in the upper troposphere (Fig. 12f) also occur in this region. This suggests that the mechanism outlined by Minobe et al. (2008) functions much more efficiently in HRC06 than in LRC07.

4.2 Summer pattern

We have also examined the seasonal changes of these variables. In general, the fall and winter patterns are very similar to that in the annual means described above. The patterns in the spring and summer, however, suggest some qualitative differences in the scenario. In this subsection, we analyze the mechanisms of the summer precipitation pattern in the GS region.

As we have pointed out in Sect. 3.1, a major seasonal change of the GS precipitation is a southwestward shift of the main rain belt from winter to summer. Figure 13 shows the upper level divergence from the summer (JJA) season and the boundary layer convergence generated by the SST gradient, as represented by the SLP Laplacian from the ERA-Interim analysis and the Athena T159 and T1279 simulations. Comparing with the corresponding panels of Fig. 2c, g, o, it can be seen that the upper level divergence (Fig. 13a–c) matches very well with the major precipitation centers over the Florida Current and the western GS where the SST is relatively higher. The SST gradient induced surface convergence from the observations (Fig. 13d), which forms a narrow band over the warm side of the SST front, contributes to the upper level divergence and accounts for the divergence center (Fig. 13a), where the strongest precipitation occurs. On the other hand, the patterns of the upper level divergence and the SST gradient induced boundary layer convergence, as represented by the Laplacian of SLP, has larger differences, in comparison to the more consistent patterns between them in annual means. In particular, the area of the 500–200 hPa mean divergence is broader over

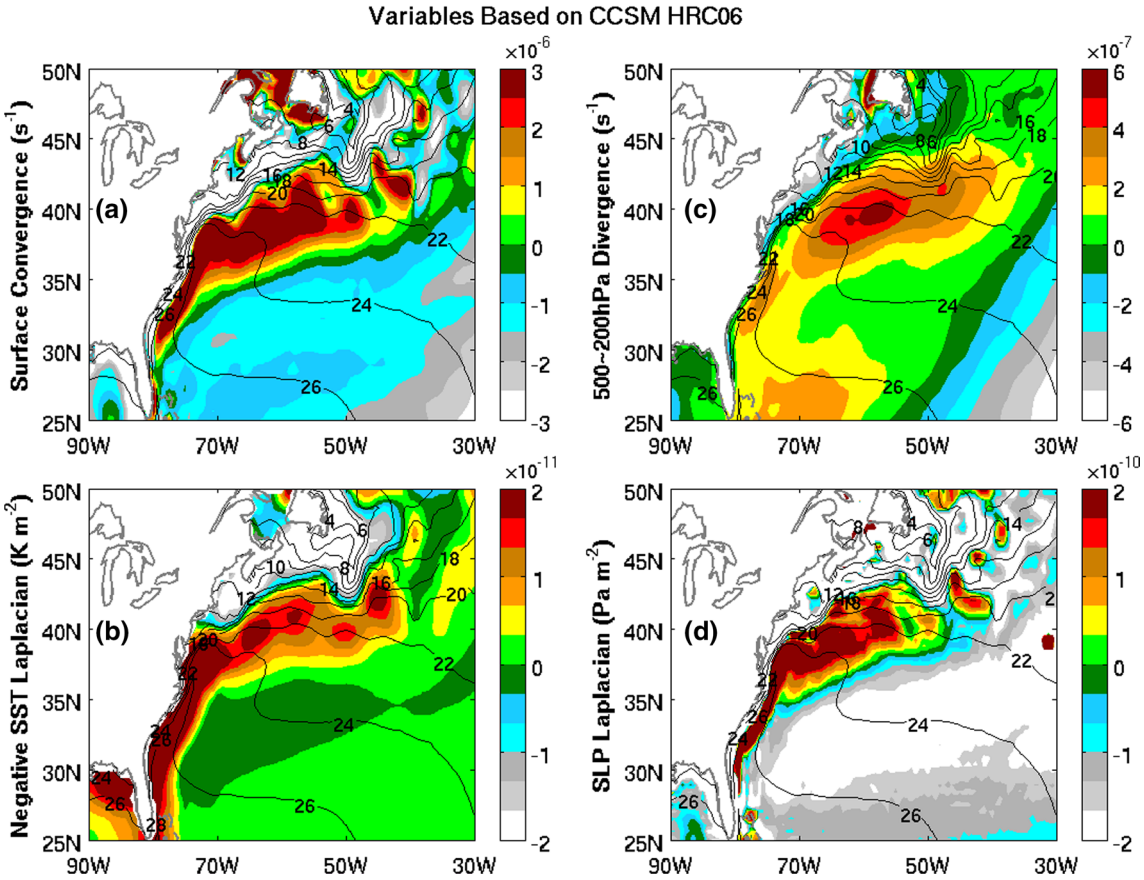

Fig. 11 *Shadings*: climatology of **a** surface convergence (unit: s^{-1}), **b** negative laplacian of SST (unit: °C m^{-2}), **c** 500–200 hPa divergence (unit: s^{-1}) and **d** the SLP laplacian (unit: Pa m^{-2}) based on CCSM3.5 HRC06. The corresponding *color bar* is on the *right of each panel*. The model SST climatology (°C) is overlaid as *contours in each panel*. The contour interval is 2 °C

the tropical-subtropical ocean and more organized than the boundary layer convergence. Moreover, the summer upper level divergence is stronger than the annual mean one (Fig. 7c), although the surface convergence in summer (not shown) is weaker than the corresponding annual mean. The weakening of the boundary layer divergence from winter to summer is consistent with the weaker SST gradient across the oceanic front in the GS extension during summer. We speculate that, as the SST gradient weakens, the upper level divergence is shifted southwestward over the Florida Current and the western Gulf Stream, where deeper convection may be generated over the warmer water with a more elevated heat source in the mid-atmosphere. In fact, Minobe et al. (2010) have pointed out that deep convection mainly occurs in summer over the Florida Current and the western Gulf Stream. It is interesting to note that, even in the annual mean state, the main precipitation band and the upper level divergence are shifted southwestward toward the Florida Current and the western Gulf Stream in LRC07 because the SST gradient is weaker in the GS extension.

Similar structural differences between the upper and lower levels can also be seen from the Athena simulations. In the models, a deep-layer convergence over the warm water may play a more important role because the SST gradient induced boundary layer convergence is more disorganized (Fig. 13e, f). The JJA differences between the T1279 and T159 runs (Fig. 14) shows that the AGCM resolution increase mainly enhances the surface convergence (Fig. 14b, c) and upper level divergence (Fig. 14a) near the SST front, which enhance the precipitation (Fig. 14d), especially the stratiform precipitation (Fig. 14f). However, the effect of the AGCM resolution increase is quite modest with respect to the magnitude of precipitation.

5 Summary

Using simulations from different climate models, we have investigated the influence of horizontal resolution in atmospheric and oceanic model components on the simulated

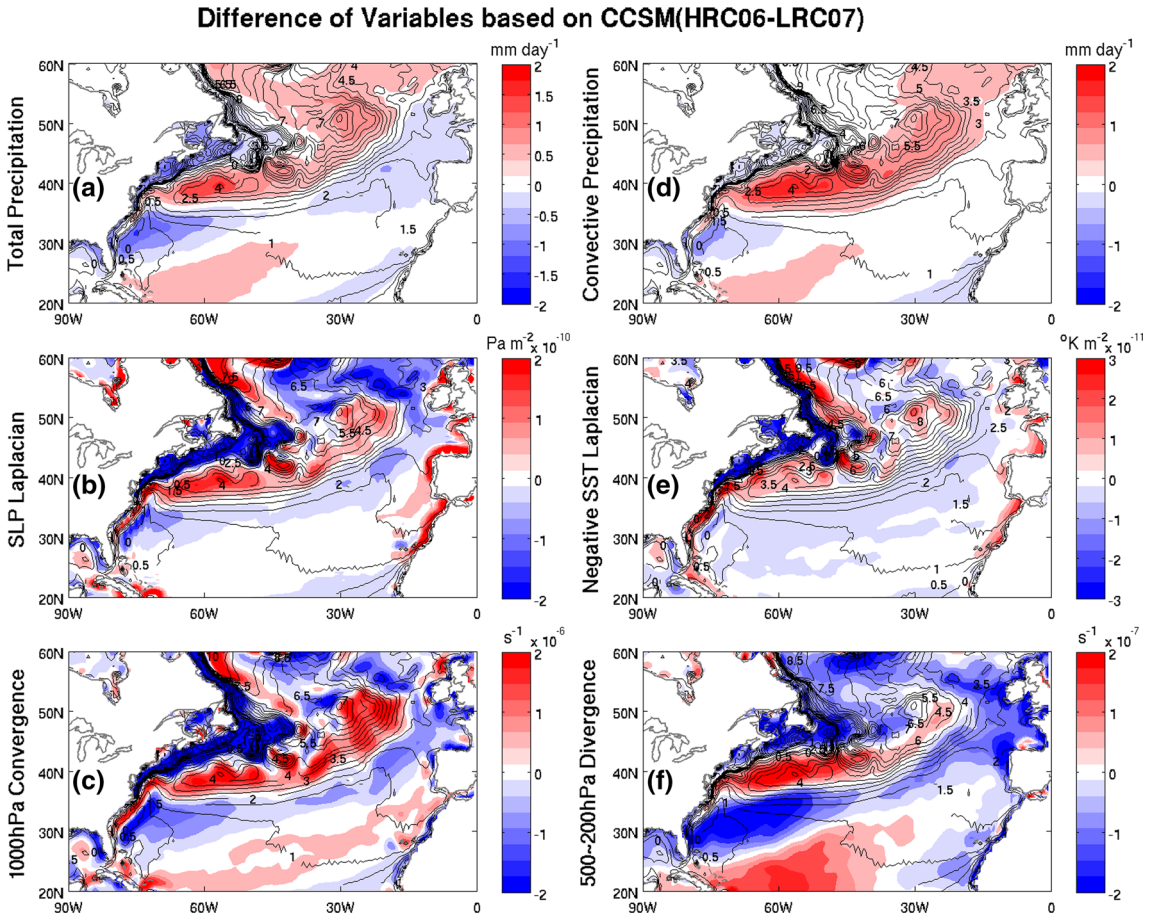

Fig. 12 Climatological differences (*shadings*) between the CCSM3.5 HRC06 and LRC07 simulations. The SST climatology differences (°C) are overlaid as *contours on all panels*. Difference is defined as HRC06–LRC07. The order of this figure is **a** total precipitation climatology (unit: mm day^{-1}), **b** SLP laplacian (unit: Pa m^{-2}), **c** 1000 hPa convergence (c; unit: s^{-1}), **d** convective precipitation (unit: mm day^{-1}), **e** negative SST laplacian (unit: °C m^{-2}) and **f** 500–200 hPa divergence (unit: s^{-1}). The *shading scales* are on the *right side* of their corresponding *panels*

mean precipitation over the Gulf Stream (GS) region. In particular, three sets of model simulations are analyzed. The first two examine the effects of increasing horizontal resolution of an AGCM gradually from around 100 to near 10 km under two fixed oceanic settings. Specifically, the AGCM is either forced with prescribed observed SST in the first case, or coupled to an OGCM at a fixed horizontal resolution near 100 km that is not eddy resolving in the second case. The third set of experiments examines the effects of the oceanic resolution with a pair of long-term simulations using another CGCM, in which the OGCM is run respectively at non-eddy-resolving (100 km) and eddy-resolving (10 km) resolutions, while the AGCM resolution remains fixed at around 50 km for both runs.

The Gulf Stream in the North Atlantic is associated with a narrow rain belt that is attached to the tight SST gradient associated with the oceanic front, according to observations. Seasonally, there is clear annual cycle with main precipitation concentrated near the GS extension and NAC track in boreal fall and winter and retreated southwestward to the Florida Current and the western GS. Our results show that all simulations reproduce qualitatively these gross features of the mean GS precipitation and its annual cycle. At similar AGCM resolutions, the uncoupled models produce more realistic GS rain band in both structure and strength than the coupled models with non-eddy-resolving oceans do. This is because the prescribed observed SST better represents the gradient near the oceanic front than the non-eddy-resolving OGCMs simulate although both are nominally generated on a 1° × 1° resolution. An increase from the baseline AGCM resolution yields enhanced GS precipitation climatology in both large-scale and convective precipitation in the North Atlantic, with the latter more tightly confined to the oceanic front. The enhancement, however, is moderate and further increase in resolution achieves diminishing results. On the other hand, an increase in oceanic resolutions from non-eddy-resolving to eddy resolving regimes result in more consistent simulations

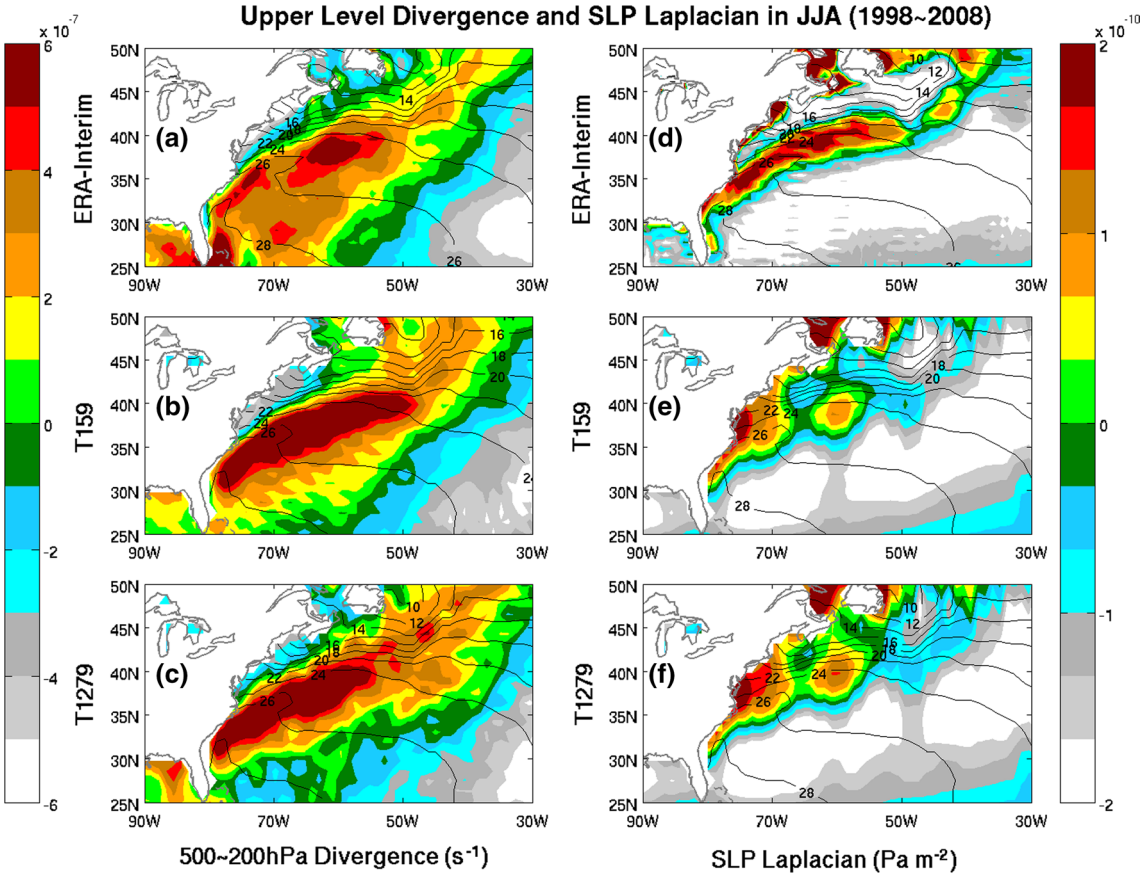

Fig. 13 The *shadings* in the *left panels* show the JJA climatologies of the 500–200 hPa divergence (unit: s^{-1}) for **a** ERA-Interim, **b** Athena T159 and **c** Athena T1279. The corresponding *shading* scale is on the left of these *panels*. The *shadings* in the *right panels* show the JJA climatologies of the SLP laplacian (unit: Pa m^{-1}) for **d** ERA-Interim, **e** Athena T159 and **f** Athena T1279. The corresponding *shading scale* is on the *right* of these *panels*. The JJA climatologies of SST the ERA-Interim data and the Athena simulations are superimposed as contours with 2 °C interval on the corresponding *panels*

with observations in both intensity and structure of the rain band. The major increase is in the convective precipitation near the much-tightened SST gradient associated with the oceanic front. Therefore, increasing from current base resolutions, the intensity improvement caused by oceanic resolution increases is more effective than that from atmospheric resolution increases.

Further analyses show that the improvement of Gulf Stream precipitation climatology due to model horizontal resolution increases can be understood in terms of the atmospheric surface pressure adjustment to sharper SST gradient near the oceanic front, which leads to stronger atmospheric convergence in the atmospheric boundary layer. The ascending motion at the top of the boundary layer seems to affect the upper level divergence. This associated ascending motion contributes to the precipitation band located in the Gulf Stream. Our result also shows that this mechanism is most effective in the winter circulation. During the summer, the convections over the warm water of the Florida Current and the western Gulf Stream seem to play a stronger role in enhancing the upper level divergence, in addition to the SST gradient induced boundary layer convergence.

Our results are based on a comprehensive examination of several model simulations in both coupled and uncoupled settings. This is because it is hard to use a single system to conduct such a wide range of simulations to test the sensitivity of both the atmospheric and oceanic resolutions in a variety of settings and combinations. One caveats of this approach is that factors other than the resolution may contribute to the model differences we have discussed here. For instance, the relatively weak GS precipitation in the CCSM3.5 LRC07, in comparison to the Minerva runs (e.g., T319), is possibly because the former also has fewer vertical levels to resolve the highly baroclinic vertical structures in this region. On the other hand, we find from the analysis of these different models a coherent picture of the influence of model resolution on the simulation in this region and the basic mechanisms that explain the behavior.

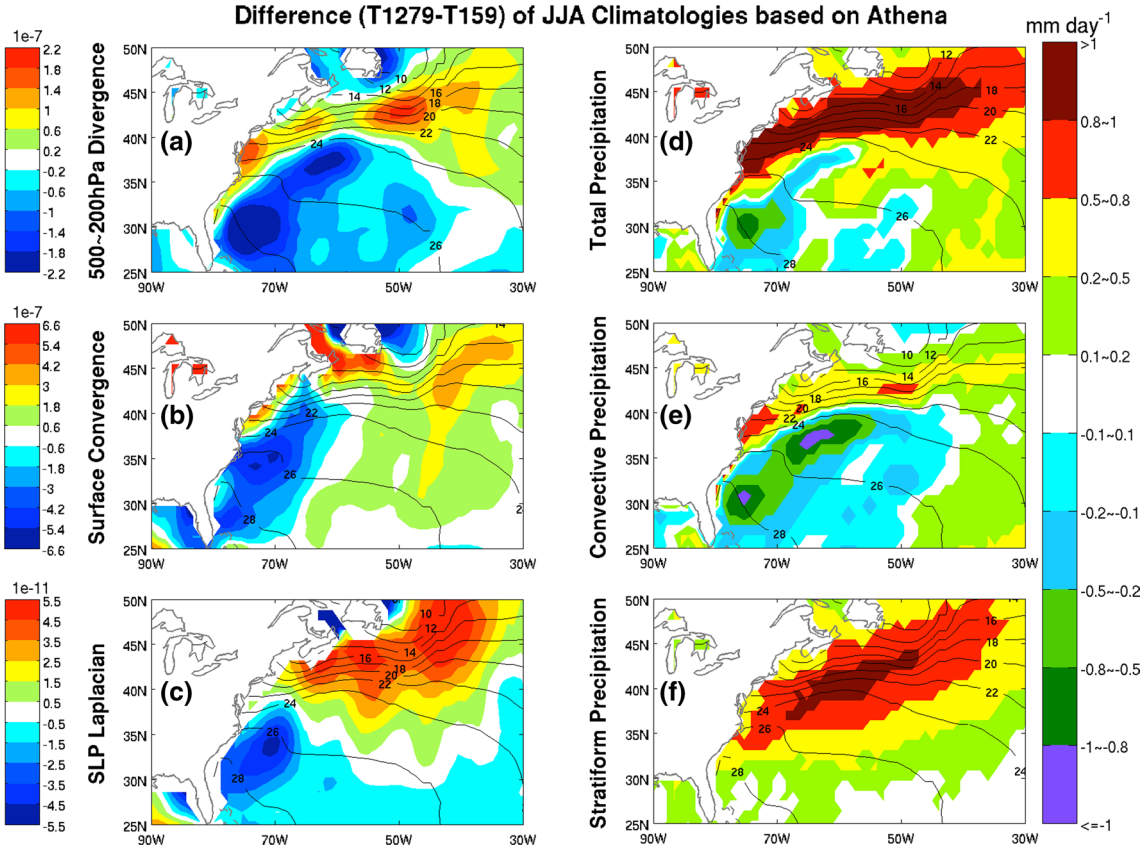

Fig. 14 *Shadings*: JJA climatological differences (Athena T1279–T159) of **a** 500–200 hPa divergence (unit: s^{-1}), **b** surface convergence (unit: s^{-1}), **c** the SLP laplacian (unit: Pa m^{-2}), **d** total precipitation, **e** convective precipitation and **f** stratiform precipitation. The unit of precipitation is (unit: mm day^{-1}). The corresponding *color bars* are on the *left side* of *left panels*. The *color bar* for precipitation is on the *right side of the right column*. The SST climatology (°C) from T159 is overlaid as contours in *each panel*. The contour interval is 2 °C

Acknowledgments XF, BH and JK are supported by Grants from NSF (AGS-1338427), NOAA (NA14OAR4310160), and NASA (NNX14AM19G). BK is supported from NSF (OCE-1419569; OCE-1154986) and ONR (N000141310844, N000141410088). We are grateful for the Athena and Minerva projects to provide climate simulations and hindcasts used in this study. XF and BH also thank Dr. C. Stan for many useful guidance and suggestions on this work.

Compliance with ethical standards

Conflict of interest The authors declare that they have no conflict of interest.

References

Barsugli JJ, Battisti DS (1998) The basic effects of atmosphere–ocean thermal coupling on mid-latitude variability. J Atmos Sci 55:477–493

Brankovic C, Gregory D (2001) Impact of horizontal resolution on seasonal integrations. Clim Dyn 18:123–143

Brayshaw DJ, Hoskins B, Blackburn M (2008) The storm track response to idealized SST perturbations in an aqua- planet GCM. J Atmos Sci 65:2842–2860

Brown AR (2004) Resolution dependence of orographic torques. Quart J R Meteor Soc 130:3029–3046

Bryan FO, Hecht MW, Smith RD (2007) Resolution convergence and sensitivity studies with North Atlantic circulation models. Part I: the western boundary current system. Ocean Model 16:141–159

Bryan FO, Tomas R, Dennis JM, Chelton DB, Loeb NG, McClean JL (2010) Frontal-scale air–sea interaction in high-resolution coupled climate models. J Clim 23:6277–6291

Chassignet EP, Marshall DP (2008) Gulf Stream separation in numerical ocean models. Ocean modeling in an eddying regime. Geophys Monogr 177:39–62

Chelton DB (2005) The impact of SST specification on ECMWF surface wind stress fields in the Eastern Tropical Pacific. J Clim 18:530–550

Chelton DB, Wentz FJ (2005) Global microwave satellite observations of sea surface temperature for numerical weather prediction and climate research. Bull Am Meteor Soc 86:1097–1115

Chelton DB, Xie SP (2010) Coupled ocean-atmosphere interaction at oceanic mesoscales. Oceanography 23(4):52–69. doi:10.5670/oceanog.2010.05

Craig A, Vertenstein M, Jacob R (2011) A new flexible coupler for earth system modeling developed for CESM4 and CESM1. Int J High Perf Comput Appl 26:31–42. doi:10.1177/1094342011428141

Frankignoul C (1985) Sea surface temperature anomalies, planetary waves, and air-sea feedback in the middle latitudes. Rev Geophys 23:357–390

Gent PR et al (2010) Improvements in a half-degree atmosphere/land version of the CCSM. Clim Dyn 34:819–833

Hack JJ, Caron JM, Danabasoglu G, Oleson KW, Bitz C, Truesdale JE (2006) CCSM–CAM3 climate simulation sensitivity to changes in horizontal resolution. J Clim 19:2267–2289

Hand R, Keenlyside N, Omrani NE, Latif M (2014) Simulated response to inter-annual SST variations in the Gulf Stream region. Clim Dyn 42:715–731. doi:10.1007/s00382-013-1715-y

Huffman GJ, Adler RF, Bolvin DT, Nelkin EJ (2010) The TRMM multi-satellite precipitation analysis (TMPA), in Satellite Rainfall Applications for Surface Hydrology, 3-22. Hossain F, Gebremichael M (Eds) Springer ISBN 978-90-481- 2914-0

Jung T et al (2012) High-resolution global climate simulations with the ECMWF model in Project Athena: experimental design, model climate, and seasonal forecast skill. J Clim 25:3155–3172

Kiehl JT, Gent PR (2004) The community climate system model, Version 2. J Clim 17:3666–3682

Kinter JL III et al (2013) Revolutionizing climate modeling with Project Athena: a multi-institutional, international collaboration. Bull Am Meteor Soc 94:231–245

Kirtman BP et al (2012) Impact of ocean model resolution on CCSM climate simulations. Clim Dyn 39:1303–1328. doi:10.1007/s00382-012-1500-3

Kobayashi C, Sugi M (2004) Impact of horizontal resolution on the simulation of the Asian summer monsoon and tropical cyclones in the JMA global model. Clim Dyn 23:165–176

Lin SJ, Rood RB (1997) An explicit flux-form semi-Lagrangian shallow water model on the sphere. Quart J R Meteor Soc 123:2477–2498

Lindzen RS, Nigam RS (1987) On the role of sea surface temperature gradients in forcing low level winds and convergence in the tropics. J Atmos Sci 44:2418–2436

Madec G (2008) NEMO reference manual, ocean dynamics component: NEMO-OPA. Preliminary version. IPSL Note du Pole de modélisation 27

May W, Roeckner E (2001) A time-slice experiment with the ECHAM4 AGCM at high resolution: the impact of horizontal resolution on annual mean climate change. Clim Dyn 17:407–420

Minobe S, Kuwano-Yoshida A, Komori N, Xie SP, Small RJ (2008) Influence of the Gulf Stream on the troposphere. Nature 452:206–209

Minobe S, Kuwano-Yoshida A, Miyashita M, Tokinaga H, Xie SP (2010) Atmospheric response to the Gulf Stream: seasonal variations. J Clim 23:3699–3719

Molteni F, Stockdale T, Balmaseda M, Balsamo G, Buizza R, Ferranti L, Magnusson L, Mogensen K, Palmer T, Vitart F (2011) The new ECMWF seasonal forecast system (System 4). ECMWF Technical Memorandum 656

Nakamura H, Sampe T, Tanimoto Y, Shimpo A (2004) Observed associations among storm tracks, jet streams, and mid-latitude oceanic fronts. Earth's Climate: The Ocean-Atmosphere Interaction. Geophys Monogr 147:329–345

Navarra A, Gualdi S, Masina S, Behera S, Luo JJ, Masson S, Guilyardi E, Delecluse P, Yamagata T (2008) Atmospheric horizontal resolution affects tropical climate variability in coupled models. J Clim 21:730–750

O'Neill LW, Chelton DB, Esbensen SK, Wentz FJ (2005) High-resolution satellite measurements of the atmospheric boundary layer response to SST variations along the Agulhas Return Current. J Clim 18:2706–2723

Pope V, Stratton R (2002) The processes governing horizontal resolution sensitivity in a climate model. Clim Dyn 19:211–236

Rayner NA, Parker DE, Horton EB, Folland CK, Alexander LV, Powell DP, Kent EC, Kaplan A (2003) Global analyses of sea surface temperature, sea ice, and night marine air temperature since the late nineteenth century. J Geophys Res 108:4407. doi:10.1029/2002JD002670

Reynolds RW, Rayner NA, Smith TM, Stokes DC, Wang W (2002) An improved in situ and satellite SST analysis for climate. J Clim 15:1609–1625

Reynolds RW, Smith TM, Liu C, Chelton DB, Casey KS, Schlax MG (2007) Daily high-resolution blended analyses for sea surface temperature. J Clim 20:5473–5496

Sampe T, Hisashi N, Atsushi G, Wataru O (2010) Significance of a midlatitude SST frontal zone in the formation of a storm track and an eddy-driven westerly jet. J Clim 23:1793–1814

Schneider N, Qiu B (2015) The atmospheric response to weak sea surface temperature fronts. J Atmos Sci 72:3356–3377

Small RJ, Tomas RA, Bryan FO (2014) Storm track response to ocean fronts in a global high-resolution climate model. Clim Dyn 43:805–828

Song Q, Cornillon P, Hara T (2006) Surface wind response to oceanic fronts. J Geophys Res 111:C12006. doi:10.1029/2006JC003680

Song Q, Chelton DB, Esbensen SK, Thum N, O'Neill LW (2009) Coupling between sea surface temperature and low-level winds in mesoscale numerical models. J Clim 22:146–164

Sweet WR, Fett R, Kerling J, Violette PL (1981) Air-sea interaction effects in the lower troposphere across the north wall of the Gulf Stream. Mon Wea Rev 109:1042–1052

Thiébaux J, Rogers E, Wang W, Katz B (2003) A new high-resolution blended real-time global sea surface temperature analysis. Bul Am Meteorol Soc 84:645–656

Uppala S et al (2005) The ERA-40 Re-Analysis. Quart J R Meteor Soc 131:2961–3012

Wai M, Stage SA (1989) Dynamical analysis of marine atmospheric boundary layer structure near the Gulf Stream oceanic front. Quart J R Meteor Soc 115:29–44

Warner TT, Lakhtakia MN, Doyle JD, Pearson RA (1990) Marine atmospheric boundary layer circulations forced by Gulf Stream sea surface temperature gradients. Mon Wea Rev 118:309–323

Wettstein JJ, Wallace JM (2010) Observed patterns of month-to-month storm track variability and their relationship to the background flow. J Atmos Sci 67:1420–1437. doi:10.1175/2009JAS3194.1

Xie SP (2004) Satellite observations of cool ocean-atmosphere interaction. Bull Am Meteor Soc 85:195–208

Zhu J (2015) ENSO prediction in Project Minerva: sensitivity to Atmospheric Horizontal Resolution and Ensemble Size. J Clim 28:2080–2095